

Experimental 4D-Var assimilation of SYNOP rain gauge data at ECMWF

Philippe Lopez

Research Department

To be submitted to the Monthly Weather Review

January 2012

This paper has not been published and should be regarded as an Internal Report from ECMWF.

Permission to quote from it should be obtained from the ECMWF.



Series: ECMWF Technical Memoranda

A full list of ECMWF Publications can be found on our web site under:

<http://www.ecmwf.int/publications/>

Contact: library@ecmwf.int

©Copyright 2012

European Centre for Medium-Range Weather Forecasts
Shinfield Park, Reading, RG2 9AX, England

Literary and scientific copyrights belong to ECMWF and are reserved in all countries. This publication is not to be reprinted or translated in whole or in part without the written permission of the Director-General. Appropriate non-commercial use will normally be granted under the condition that reference is made to ECMWF.

The information within this publication is given in good faith and considered to be true, but ECMWF accepts no liability for error, omission and for loss or damage arising from its use.

Abstract

Four-dimensional variational data assimilation (4D-Var) experiments with 6-hourly rain gauge accumulations observed at synoptic stations around the globe have been run over several months, both at high resolution in an ECMWF operations-like framework and at lower resolution in an early or mid-20th-century reanalysis style with the reference observational coverage reduced to surface pressure data only. The key aspects of the technical implementation of rain gauge data assimilation in 4D-Var are described, which includes the specification of observation errors, bias correction procedures, screening and quality control.

Results from experiments indicate that the positive impact of rain gauges on forecast scores remains limited in the operations-like context because of their competition with all other observations already available. In contrast, when only synoptic station surface pressure observations are assimilated in the reanalysis-like control experiment, the additional assimilation of rain gauge measurements substantially improves not only surface precipitation scores, but also analysis and forecast scores of temperature, geopotential, wind and humidity at most atmospheric levels and for forecast ranges up to 10 days. The verification against Meteosat infrared imagery also shows a clear improvement in the spatial distribution of clouds. This suggests that assimilating rain gauge data available during data sparse periods of the past might help to improve the quality of future reanalyses and subsequent forecasts.

1 Introduction

Over the last decades, progress in data assimilation (DA) techniques combined with the availability of new observation types have led to substantial improvements in our ability to represent the three-dimensional atmospheric state (temperature, humidity, wind, surface pressure,...) at any given time. The resulting *analyses* are often used in operational numerical weather prediction (NWP) to initialize global or limited-area model forecasts over a large variety of time ranges. Operational weather forecasts over periods of up to 10 days have been shown to benefit from improved atmospheric analyses (i.e. initial conditions). In addition to operational DA, which works with real-time observations, it is also possible to run data assimilation over past periods to produce so-called reanalyses. Benefits of the latter lie in the possibility to use extra observations that were not available in real-time and to take advantage of a posteriori improvements of the data assimilation system. For instance, ECMWF (see Appendix 1 for list of acronyms) run their operational DA system twice daily to generate analyses and 10-day forecasts, but also utilized a similar system to produce global atmospheric and surface reanalyses for the period 1957-2002 (ERA40; Uppala *et al.* 2005).

A commonly used DA method is the variational method (e.g. Le Dimet and Talagrand 1986) which searches for the model state that best fits a set of available observations and some a priori (or *background*) information from the model, in a least-square sense. Temperature, wind and surface pressure observations were first to be successfully assimilated, later followed by water vapour measurements.

Since the late 1990s, significant efforts have been devoted to the assimilation of observations that are directly related to clouds and precipitation. As far as satellite platforms are concerned, the assimilation of microwave brightness temperatures from SSM/I or precipitation retrievals from the latter was implemented in several operational systems worldwide (Treadon *et al.* 2002; Marécal and Mahfouf 2003; Lin *et al.* 2007; Bauer *et al.* 2010; Geer *et al.* 2010), using the variational assimilation approach. Experimental studies were also conducted with infrared brightness temperatures (Vukicevic *et*

al. 2006), cloud optical depths (from MODIS; Benedetti and Janisková 2008), precipitation radar reflectivities (from TRMM-PR; Benedetti *et al.* 2005) and cloud radar data (from CloudSat; Janisková *et al.* 2011), among others. From the prospect of ground-based instruments, the assimilation of reflectivities or rainfall retrievals obtained from precipitation radars is already operational in the limited area models of several weather forecasting centres (Macpherson 2001; Ducrocq *et al.* 2002; Caumont *et al.* 2010), using either latent heat nudging, diabatic initialization or a mixed Bayesian-variational method, respectively. Furthermore, direct four-dimensional variational (4D-Var) DA of surface rain data from ground-based radars recently became operational in ECMWF’s global forecasting system (Lopez 2011). In a more experimental context, the assimilation of ground-based radar data on the mesoscale using the alternative technique of ensemble Kalman filtering was studied by Tong and Xue (2005) and Caya *et al.* (2005).

Taking advantage of all the developments made at ECMWF for the direct 4D-Var assimilation of NCEP Stage IV ground-based radar data (Lopez 2011), which became operational on 15 November 2011, the present study investigates the potential benefits of directly assimilating synoptic station (SYNOP) rain gauge (RG) observations in ECMWF’s 4D-Var system. Both a high-resolution operations-like context and a lower-resolution reanalysis-like framework (with data-sparse conditions) are considered.

SYNOP RG observations assimilated in this work, the specification of their error statistics and the procedure for their bias correction are detailed in section 2. Section 3 introduces the 4D-Var assimilation method and provides additional information about quality control. Results from direct 4D-Var assimilation experiments are presented in section 4, while remaining issues are discussed in section 5. Section 6 summarizes the main findings of this study and gives an outlook on the future of RG data assimilation at ECMWF.

2 SYNOP rain gauge observations

The precipitation data used in this study are 6-hourly accumulations ($RR6h$) measured by the worldwide network of synoptic stations. These data are routinely received at ECMWF through the Global Telecommunication System (GTS). Before the assimilation in 4D-Var, all valid SYNOP RGs available inside a model grid box are averaged into a single “superob” attached to this grid box. A logarithmic transform, $\ln(RR6h + 1)$, is also applied to each superob, since this makes the distribution of background departures closer to Gaussian (Mahfouf *et al.* 2007; Lopez 2011), as required in variational DA. Note that the 6-hourly rain accumulation used in $\ln(RR6h + 1)$ is expressed in mm h^{-1} . The following subsections will introduce the specification of observation error statistics, bias correction and screening procedures applied to SYNOP RGs.

2.1 Rain gauge errors

Rain gauge measurements can be affected by a large variety of both systematic and random errors.

2.1.1 Systematic errors

Systematic errors are dominated by wind-induced errors which result from the deformation of the airflow by the gauge itself. Wind-induced error usually causes precipitation undercatch and thus a negative bias in the observations. This type of error will be addressed in subsection 2.2 dealing with bias-correction.

Other systematic errors can be attributed to the wetting of the gauge walls, to the loss through evaporation (especially for manual RGs) and to raindrops splashing away from the gauge collector. All can lead to an additional underestimation of precipitation by RGs, the magnitude of which is usually well below 0.1 mm h^{-1} though (Sevruk 1974a; Sevruk 1974b). It will thus be neglected in this study.

2.1.2 Local random errors

RG measurements can also be affected by local random errors, caused for instance by the discrete nature of the time sampling in tipping bucket RGs, by small-scale variations of the turbulent airflow around the gauge, or even by occasional blockage of the gauge collector. To account for these errors, which usually significantly decrease with accumulation length (Ciach 2003), a fixed contribution $\sigma_{loc} = 0.05$ in terms of $\ln(RR6h + 1)$ has been used in all experiments. These errors are usually much smaller than representativity errors described in the next subsection.

2.1.3 Representativity errors

Representativity errors arise every time rain gauge point measurements need to be compared with model grid-box averaged precipitation fields, as in the context of data assimilation. In this work, the choice has been made to average (or "superob") SYNOP RG observations onto the model grid before starting the assimilation process. In practice, representativity error can be quantified by the standard deviation of the horizontal fluctuations of surface precipitation over the model grid-box area. For a single gauge, representativity error increases with model grid-box size as well as in the presence of convective precipitation (higher spatial variability). When several RGs can be averaged inside a model grid box, the resulting representativity error is expected to drop, since multiple measurements usually provide more information than a single one.

Here, RG representativity error has been specified using the simple parametrization proposed by Lopez *et al.* (2011), which was derived from ground-based radar precipitation estimates and local high-density RG networks and which is applied in terms of $\ln(RR6h + 1)$. The representativity error standard deviation, σ_{rep} , is parametrized as a function of model resolution and day of the year and also includes the effect of spatial correlations among RGs that are located inside the same model grid box. The parametrized representativity errors are maximum in summer and minimum in winter, and the opposite is true for spatial correlations. This is a very crude way of taking into account the contrast between stratiform precipitation in winter (low spatial variability) and convective rainfall in summer (high spatial variability). A more detailed description of the parametrization can be found in Appendix 2. With this formulation, σ_{rep} (in terms of $\ln(RR6h + 1)$) typically ranges between 0.08 and 0.25 (resp. 0.04 and 0.13) for T511 ($\approx 40 \text{ km}$) (resp. T1279 ($\approx 15 \text{ km}$)) model resolution. The relative crudeness of the representativity error formulation will be discussed in section 5.

Eventually, this yields the total observation error standard deviation $\sigma_o = \sqrt{\sigma_{loc}^2 + \sigma_{rep}^2}$ to be applied in the data assimilation process, where σ_{loc} was defined in section 2.1.2. For illustration purposes, Fig. 1 displays the distribution of σ_o values specified in the T511 and T1279 RG assimilation experiments presented below. As expected, σ_o is dominated by representativity error at both resolutions. The few outliers with a larger error standard deviation of about 0.2 in panel (b) correspond to model grid boxes that contain a single RG (i.e. higher values of σ_{rep}).

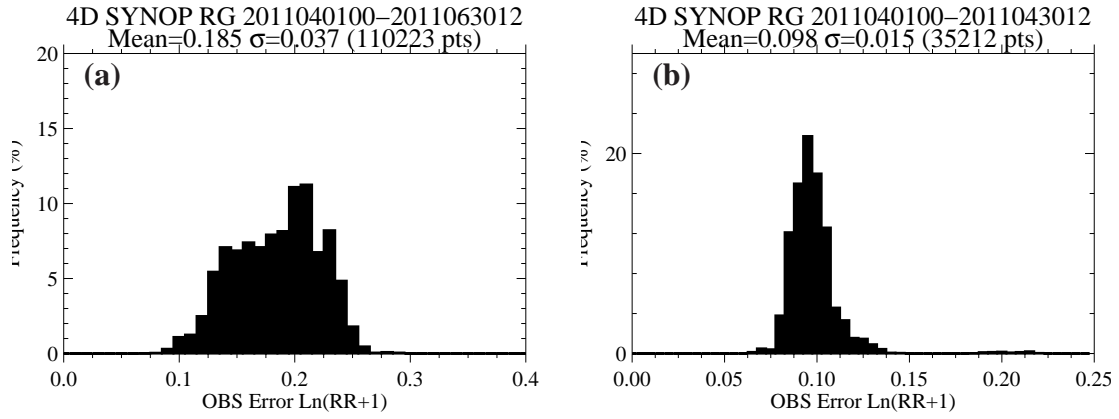


Figure 1: Total observation error histograms from the (a) T511 and (b) T1279 truncation rain gauge data assimilation experiments described in this study. Observation error values are expressed in terms of $\ln(RR6h + 1)$. Mean and standard deviation of the distribution are given at the top of each panel.

2.2 Bias correction

One of the main assumptions in variational data assimilation is that both model background and observations should be unbiased. It is therefore important to try to remove any known bias, such as that associated with wind-induced undercatch (raw SYNOP RGs are not corrected for this bias). In ECMWF's operational system, most observation types are subjected to a variational bias correction (VarBC; Dee and Uppala 2009). Here, however, a separate non-variational two-step bias correction procedure has been specially developed for RGs.

2.2.1 Correction of wind-induced error

Several studies (e.g. Folland 1988; Yang *et al.* 1998; Nešpor and Sevruk 1999) showed that wind-induced undercatch increases with wind speed and rain-gauge-top height above ground. For rain, the relative underestimation worsens as dropsize becomes smaller and is therefore much higher for drizzle than in heavy showers. For snow, wind-induced relative error is often larger than for rain and can exceed 50% in windy conditions. Therefore, RG measurements in snowy situations have been discarded in the present study. Furthermore, shielding installed around a RG can substantially reduce wind-induced error for snowfall, much less for rain.

Nešpor and Sevruk (1999) proposed a thorough study of wind-induced error for three types of RGs, two of which, Mk2 and Hellmann, are commonly used worldwide. Their work was based on wind tunnel experiments and numerical simulations of the airflow around the gauge. Here, their results have been synthesized in such way that the wind-induced relative error bias correction, BC_{wind} , (for rain only) can be parametrized as

$$BC_{wind} = \frac{RR_{obs} - RR_{true}}{RR_{obs}} \quad (1)$$

$$= a RR_{obs}^b \quad (2)$$

where coefficients a and b are power functions of the wind speed at gauge-top level, V_{RG} ,

$$a = a_1 V_{RG}^{a_2} \quad (3)$$

$$b = b_1 V_{RG}^{b_2} \quad (4)$$

Note that the coefficients of the parametrization have been computed by assuming that $\kappa = 0$ and selecting the "turbulent" case of Nešpor and Sevruk (1999). The values of parameters a_1 , a_2 , b_1 and b_2 are given in Table 1 for the two RG types considered here. As an illustration, Fig. 2 displays curves

Rain gauge type	a_1	a_2	b_1	b_2
Mk2	-0.031	0.547	-0.640	-0.085
Hellmann	-0.030	0.733	-0.631	-0.091

Table 1: Values of the parameters a_1 , a_2 , b_1 and b_2 used in Eq. (3) and Eq. (4).

of the parametrized wind-induced relative error as a function of rainfall rate, for various wind speeds at gauge-top level and for the Mk2 (panel (a)) and Hellmann (panel (b)) gauge types. Relative error clearly increases for smaller rainfall rates and stronger winds. It is also obviously higher for the larger Hellmann type than for the Mk2 type.

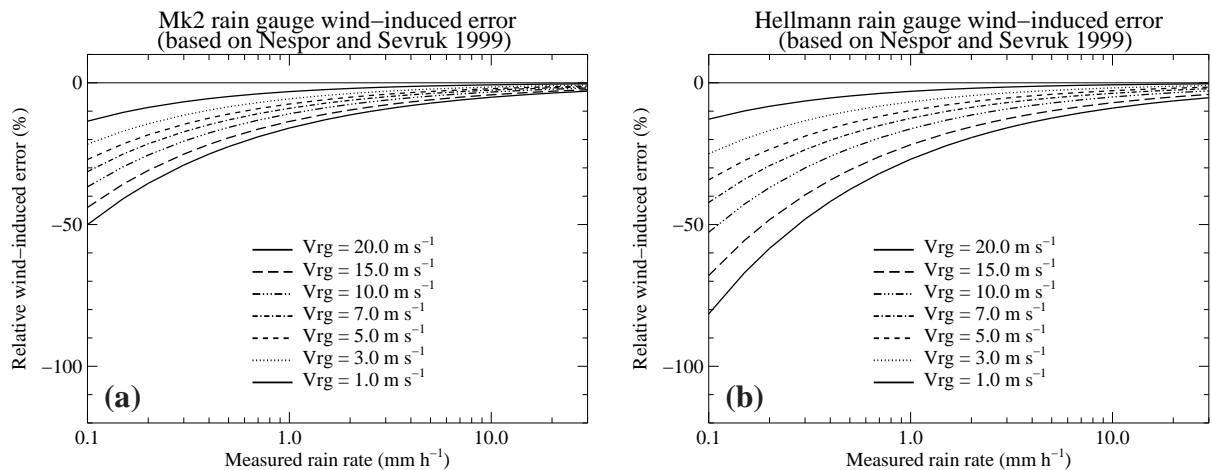


Figure 2: Curves of wind-induced relative error as a function of rainfall rate (in mm h^{-1}), for various wind speeds at gauge-top level (in m s^{-1}) and for (a) Mk2 and (b) Hellmann gauge types.

Assuming a logarithmic profile for the wind in the surface layer, one can write

$$V_{RG} = \frac{\ln(h_{RG}/z_0)}{\ln(10/z_0)} V_{10m} \quad (5)$$

where V_{10m} is the 10-m wind speed (from SYNOP reports), h_{RG} is the gauge-top height above ground and z_0 is the roughness length (set to 0.02 m here, a typical value for short-grass cover).

In the presence of rain-gauge shielding, BC_{wind} is reduced through

$$BC_{wind} = BC_{wind} \left\{ \frac{1 - 0.9631}{\pi/2} \arctan\left(\frac{0.7784}{V_{10m}}\right) + 0.9631 \right\} \quad (6)$$

which leads to a maximum reduction of about 4% of BC_{wind} in strong wind conditions.

Eventually, the bias-corrected value of the rain observation, \widetilde{RR}_{obs} , is given by

$$\widetilde{RR}_{obs} = RR_{obs}(1 - BC_{wind}) \quad (7)$$

Information about gauge type, gauge-top height and the presence of shielding was first collected from Sevruk and Klemm (1989) and was then updated through individual contacts with the major national weather services around the world. It should be stressed that, despite all these efforts, the information thereby obtained might not be completely accurate for some countries, given the absence of worldwide standards for RG specifications. As far as gauge type is concerned, for simplicity, all worldwide RGs have been categorized as either Mk2 or Hellmann, depending on their shape and size. Figure 3, Fig. 4 and Fig. 5 show global maps of gauge types, gauge-top heights and presence of shielding, respectively, as prescribed in this work. One should note that the wind-induced error bias correction is applied to each individual RG before averaging over the corresponding model grid box.

SYNOP rain gauge type: black=Mk2; red=Hellmann

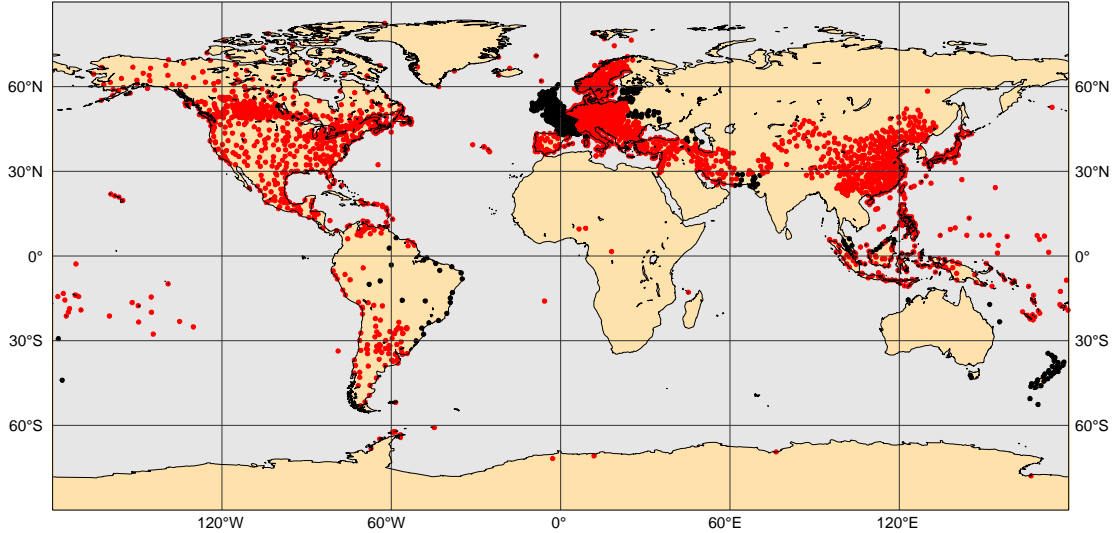


Figure 3: Global map of rain gauge types, as assumed in this study. Typical daily data coverage obtained from GTS.

2.2.2 Correction of other biases

Besides the systematic wind-induced error bias, other biases in both observations and model have been assessed by computing global statistics of observation (bias corrected for wind) minus model background departures from a passive monitoring T1279 (≈ 15 km) L91 4D-Var experiment over April-May 2011. From these two-month statistics expressed in terms of $\ln(RR6h + 1)$, the following third-degree polynomial bias correction, BC_{other} , has been constructed:

$$BC_{other} = \sum_{i=1}^3 \alpha_i \overline{\ln(RR6h + 1)}^i \quad (8)$$

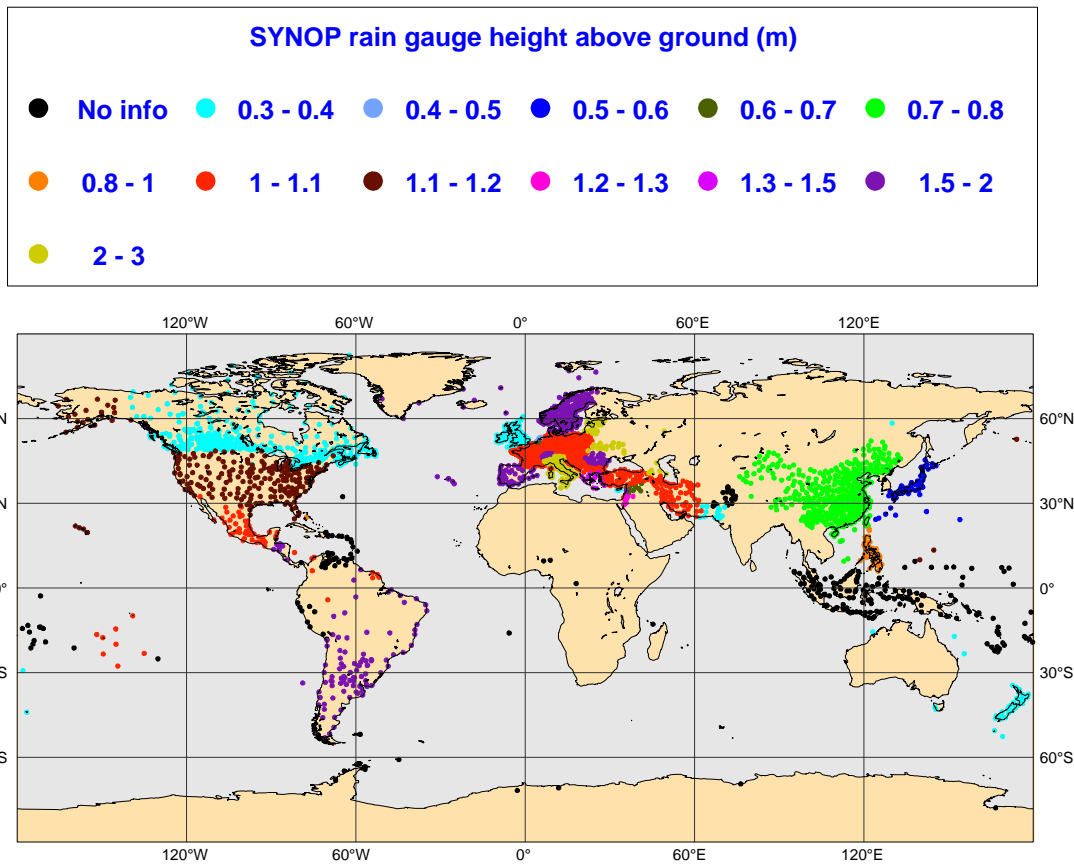


Figure 4: Same as in Fig. 3 but for rain gauge top height above ground (in m). When no information is available, gauge-top height is arbitrarily set to 1 m.

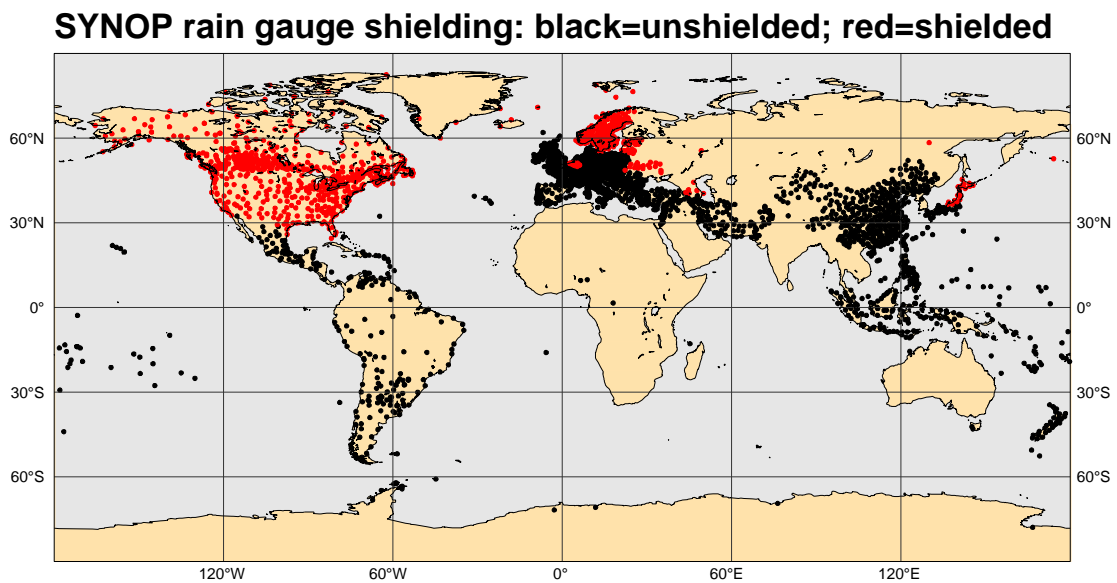


Figure 5: Same as in Fig. 3 but for rain gauge shielding.

where α_i are prescribed coefficients and $\overline{\ln(RR6h+1)}$ denotes the average over model background and observation. Using the average of model and observation avoids undesirable spurious asymmetries in the bias correction (Geer and Bauer 2011).

Figure 6 displays observation minus model background departures in terms of $\ln(RR6h+1)$ as a function of $\ln(RR6h+1)$ values in April-May 2011. The polynomial fit used to define the bias correction is also plotted (dashed line). Figure 6 illustrates the overestimation (resp. underestimation) in the model for 6-hour precipitation accumulations lower (resp. higher) than 0.6 mm h^{-1} (i.e. $\ln(RR6h+1) \approx 0.5$). The overall mean bias is rather small (-0.02 in terms of $\ln(RR6h+1)$).

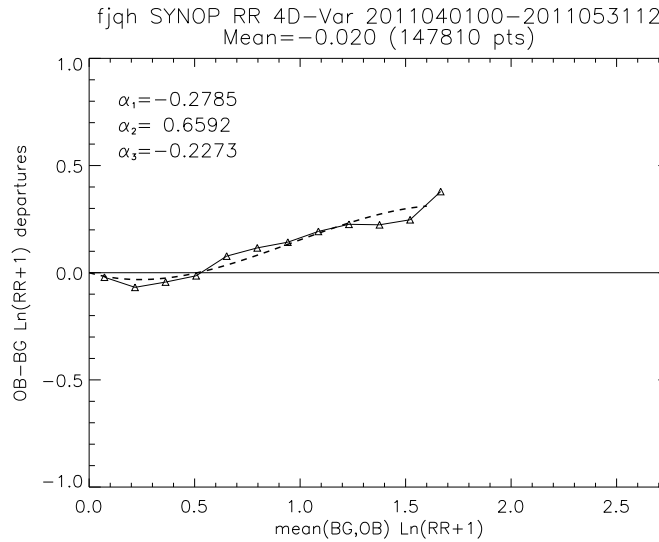


Figure 6: Average observation minus model background departures in terms of $\ln(RR6h+1)$ (solid line) as a function of $\ln(RR6h+1)$ for April-May 2011. The dash line shows the second degree polynomial fit chosen to define the bias-correction. Values of fit coefficients, α_i ($i=1, \dots, 3$), are also given.

It should be emphasized that global statistics computed for other seasons of the year yielded very similar bias curves (not shown). It is also interesting to underline the similarity of the curve shown in Figure 6 with those displayed in Lopez (2011) in the context of NCEP Stage IV ground-based radar surface rainfall data assimilation over the United States. Finally, one should note that since original SYNOP RGs are averaged onto the model grid before the assimilation, the bias correction defined in Eq. (8) is applied in model space.

2.3 Screening

In data assimilation, observations must be screened so as to reject data that are thought to be inaccurate or not representative of the model geometry. In the present case of SYNOP station RGs, the choice was made not to assimilate data:

- over rugged orography (poor horizontal representativity), i.e. wherever the standard deviation of the model subgrid-scale orography is larger than 100 m,
- when SYNOP V_{10m} exceeds 20 m s^{-1} (excessive precipitation underestimation),
- when model grid box altitude departs from SYNOP RG altitude by more than 300 m (poor vertical

representativity),

- when either SYNOP or model 2-metre temperature is below $+2^{\circ}\text{C}$ (likely snowfall),
- within the intertropical band (25°S - 25°N) (larger representativity error associated with frequent convection, as evidenced in Lopez *et al.* 2011).

It should also be mentioned that, in contrast with Lopez (2011) who rejected all ground-based rain data whenever either the model background or the observation were non-rainy, for reasons explained in his paper, no such rejection was applied in the present study. This helped to increase the number of RG data used in 4D-Var.

To illustrate the result of the screening process, an example of SYNOP rain gauge 6-hourly precipitation data coverage, after superobbing and as passed to 4D-Var in this study, is displayed in Fig. 7 at 1800 UTC 16 April 2011. In this plot, each point corresponds to a T1279 model grid box over which available valid gauges were averaged. In practice, this coverage of around 2000 observations is reduced even further during the analysis process, due to the additional quality control described in section 3.2. Most of the observations selected in this work are located over Europe, North America, China, Japan, South America, South Africa and New Zealand (but no available data over Australia). Finally, one should also keep in mind that the choice of averaging RGs over model grid boxes means that the number of observations passed to 4D-Var does increase with model resolution, but within the limit imposed by the local density of available RGs.

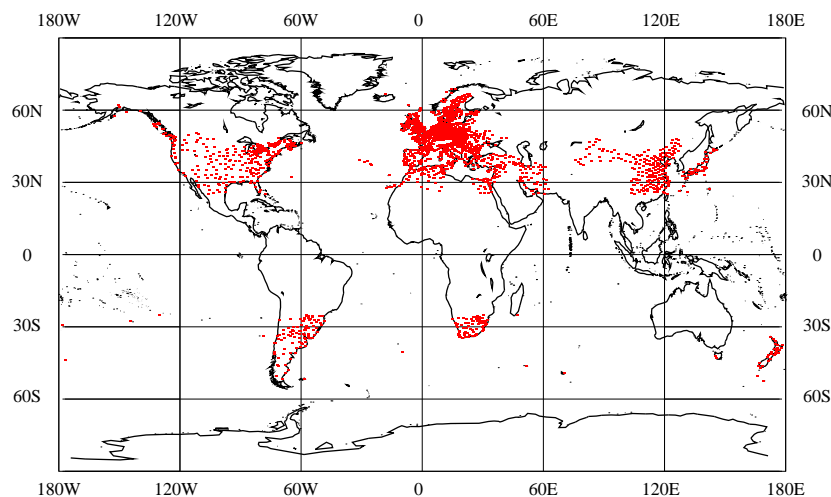


Figure 7: Example of SYNOP rain gauge 6-hourly accumulated precipitation data coverage (after superobbing) at 1800 UTC 16 April 2011 as obtained through the GTS, after screening out points affected by rugged orography, snowfall, strong surface winds, or located in the tropics.

3 The 4D-Var method

3.1 General description

The aim of 4D-Var assimilation is to find the optimal initial 3D atmospheric state (the *analysis*) that leads to a short-range model forecast that best fits a set of observations and some a priori information from the

model (the so-called *model background* or *trajectory*) over a certain time window (currently 12 hours at ECMWF). Formally, the analysis corresponds to the model state $\mathbf{x}(t_0)$ at time t_0 which minimizes the following cost function

$$\begin{aligned}
 J[\mathbf{x}(t_0)] &= \frac{1}{2} [\mathbf{x}(t_0) - \mathbf{x}^b(t_0)]^T \mathbf{B}_0^{-1} [\mathbf{x}(t_0) - \mathbf{x}^b(t_0)] \\
 &+ \frac{1}{2} \sum_{i=0}^n [H_i[M[\mathbf{x}(t_0)]] - \mathbf{y}_i^o]^T \mathbf{R}_i^{-1} [H_i[M[\mathbf{x}(t_0)]] - \mathbf{y}_i^o]
 \end{aligned} \tag{9}$$

following the notations and definitions of Ide *et al.* (1997). $\mathbf{x}^b(t_0)$ denotes the model background state at initial time. In ECMWF's 4D-Var system, the model state consists of temperature, humidity, vorticity, divergence and surface pressure. H_i and M are the often non-linear observation operator and forecast model, respectively, used for converting the initial model state to observed equivalents at time t_i . All observations available in the assimilation window are gathered in vector \mathbf{y}_i^o . \mathbf{R}_i and \mathbf{B}_0 are respectively the observation and model background error covariance matrices. \mathbf{B}_0 is made flow-dependent through a wavelet formulation (Fisher 2004).

In practice at ECMWF, J is re-formulated using an incremental approach (Courtier *et al.* 1994). In each 4D-Var cycle, three successive minimizations are performed at lower horizontal resolution. After each minimization, the model trajectory and observation–model departures are recomputed at high resolution. Starting with the lowest resolution ensures that larger scales are adjusted first, reduces the computational cost of 4D-Var and permits the handling of weak non-linearities, even though 4D-Var still strongly relies on the linearity assumption for all meteorological processes it describes.

Of particular interest for the assimilation of precipitation observations, linearized simplified parametrizations of convection (Lopez and Moreau 2005) and large-scale moist processes (Tompkins and Janisková 2004) are used during each minimization. Other linearized physical processes also accounted for are radiation (Janisková *et al.* 2002), vertical diffusion and orographic gravity wave drag (Mahfouf 1999) and non-orographic gravity wave drag (Orr *et al.* 2010).

3.2 First-guess check and variational quality control

Like all other observation types already used in 4D-Var, SYNOP RG observations are subjected to an a-priori first-guess check to reject measurements that depart too much from the model background. Here, a RG observation is rejected if $|H_i[\mathbf{x}^b(t_i)] - \mathbf{y}_i^o| > 4\sqrt{\sigma_o^2 + \sigma_b^2}$, where σ_o is the observation error standard deviation (see section 2.1) and σ_b is the background error standard deviation (set to 0.18), both expressed in terms of $\ln(RR6h + 1)$. This first-guess check for SYNOP RG data is only applied in the first trajectory of each 4D-Var cycle, as for all other observation types.

In addition, in the course of each minimization, the variational quality control (VarQC; Andersson and Järvinen 1999) already applied to all other observation types is also applied to SYNOP RG data. Any observation which leads to large departures that are deemed inconsistent with neighbouring measurements, has its weight artificially reduced in the analysis.

4 Experiments

4.1 Set-up

Two global 4D-Var baseline experiments have been considered in this work: (1) a T511 (≈ 40 km) early or mid-20th-century (future) reanalysis-like experiment with the assimilation of surface pressure (Ps) data from SYNOP land stations and ships only (ERA_CTRL hereafter) and (2) an ECMWF operation-like T1279 (≈ 15 km) run with all available observation types assimilated (OPER_CTRL, hereafter). Experiments corresponding to each baseline set-up plus SYNOP RG observations were then run to assess the impact of the additional rain gauge data on the quality of the 4D-Var analyses and subsequent 10-day forecasts (resp. ERA_NEW and OPER_NEW). All experiments were run using ECMWF model cycle 37r2 and with 91 vertical levels. Table 2 summarizes the experimental set-up in terms of spectral truncation (in both trajectory and the three 4D-Var minimizations), period and observational coverage. The choice of the spring season is justified by the desire to avoid the rejection of too many RG observations due to the occurrence of snowfall in the winter hemisphere and to properly sample both stratiform and convective rainy events in the northern hemisphere extratropics.

Experiment	Truncation		Period	Observational coverage
	Trajectory	Minimizations		
ERA_CTRL	T511	T95/T159/T255	Apr-Jun 2011	SYNOPSIS only
ERA_NEW	T511	T95/T159/T255	Apr-Jun 2011	SYNOPSIS only + SYNOPSIS RGs
OPER_CTRL	T1279	T159/T255/T255	Apr-May 2011	as in operations
OPER_NEW	T1279	T159/T255/T255	Apr-May 2011	as in operations + SYNOPSIS RGs

Table 2: Experimental set-up used in this study to assess the impact of assimilating SYNOPSIS rain gauge data in 4D-Var.

4.2 Results from ERA-like experiments

4.2.1 Coverage in assimilated observations

As preliminary information, the mean density of SYNOPSIS RG superobs that are actually assimilated in each 4D-Var cycle (i.e. every 12 hours) is displayed in Fig. 8 for the period April-June 2011. One can see that Europe, North America and China are the regions with the highest data coverage. A smaller number of RG data is also assimilated in South America, South Africa and New Zealand.

4.2.2 Background and analysis precipitation departures

As a first verification, the statistical distributions of observation–background and observation–analysis departures are plotted in Fig. 9. Probability density functions (PDF) from ERA_NEW are plotted in terms of $\ln(RR6h + 1)$ for the period April-June 2011, which yields a total sample size of 110223 (i.e. around 600 rain observations assimilated in each 4D-Var cycle on average).

Panel (a) in Fig. 9 shows that the distribution of observation–background departures after bias correction (see section 2.2) is not really exactly Gaussian (green curve), yet rather symmetrical, which is always

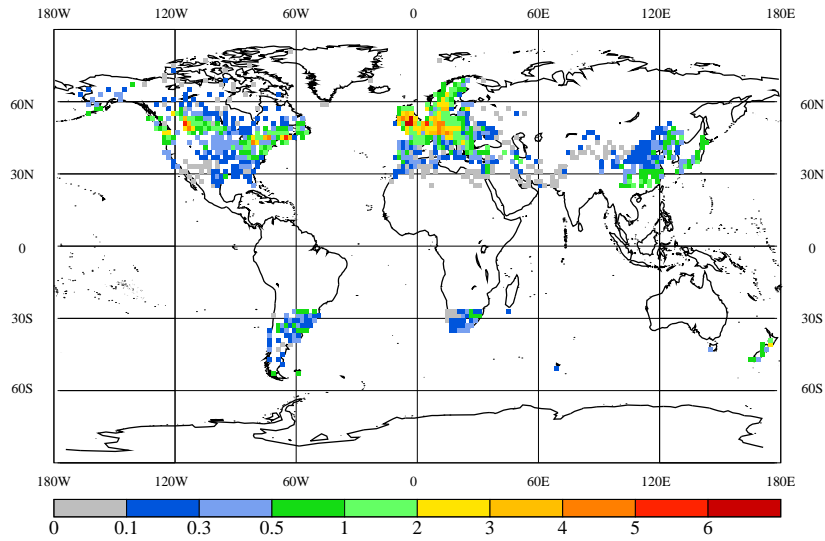


Figure 8: Mean density of assimilated SYNOP rain gauge data, expressed in superobs per $2^{\circ} \times 2^{\circ}$ grid box and per 4D-Var cycle.

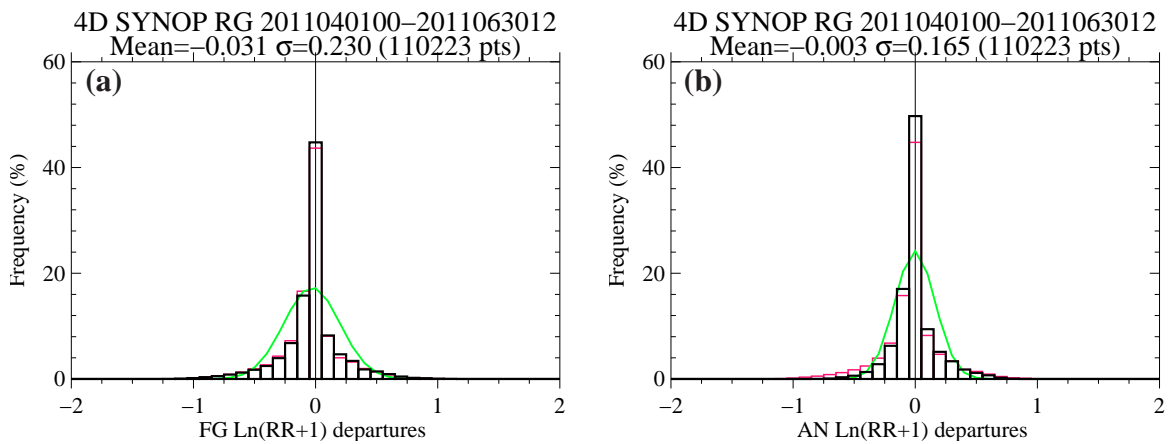


Figure 9: Histograms of (a) observation–background and (b) observation–analysis $\ln(RR6h + 1)$ departures from ERA_NEW over the period April–June 2011. Black lines display the histogram of bias-corrected background departures in panel (a) and analysis departures in panel (b). Red curves show the uncorrected background departures in panel (a) and the bias-corrected background departures in panel (b) (i.e. a copy of the black curve from the left panel). Green curves show the Gaussian distribution with the same mean and standard deviation as the black histogram. Frequency (y-axis) is in % and the mean, standard deviation (σ) and total population of the black histograms are shown at the top of each panel.

desirable. The mean $\ln(RR6h + 1)$ background departure is small (-0.031 , indicating a slightly too rainy background), while the mean analysis departure is even smaller (-0.003). Panel (b) demonstrates that the PDF of observation–analysis departures is much narrower than that of observation–background departures, with the standard deviation dropping from 0.230 down to 0.165. Analysis departures are also closer to being normally distributed. Therefore, 4D-Var succeeds in bringing the model rain closer to the observations through the changes in temperature, moisture, wind and surface pressure imposed by the assimilation of SYNOP Ps and RG information.

4.2.3 Precipitation scores against SYNOP rain gauges

Another way to check the impact of SYNOP RG assimilation in terms of surface precipitation is to compute scores against SYNOP RG data themselves, for different forecast ranges. Of course, in this approach, RG observations cannot be regarded as independent validation data for the first hours of the forecast since they are assimilated in experiment ERA_NEW, but such comparison can be useful to confirm that the 4D-Var assimilation of RGs performed as hoped. Two examples of scores computed for the entire period over Europe, the USA and China (where most RGs were assimilated) are shown in Fig. 10: Equitable Threat Score (ETS) and False Alarm Rate (FAR), as defined in Appendix 3. The higher ETS and the lower FAR, the better the forecast.

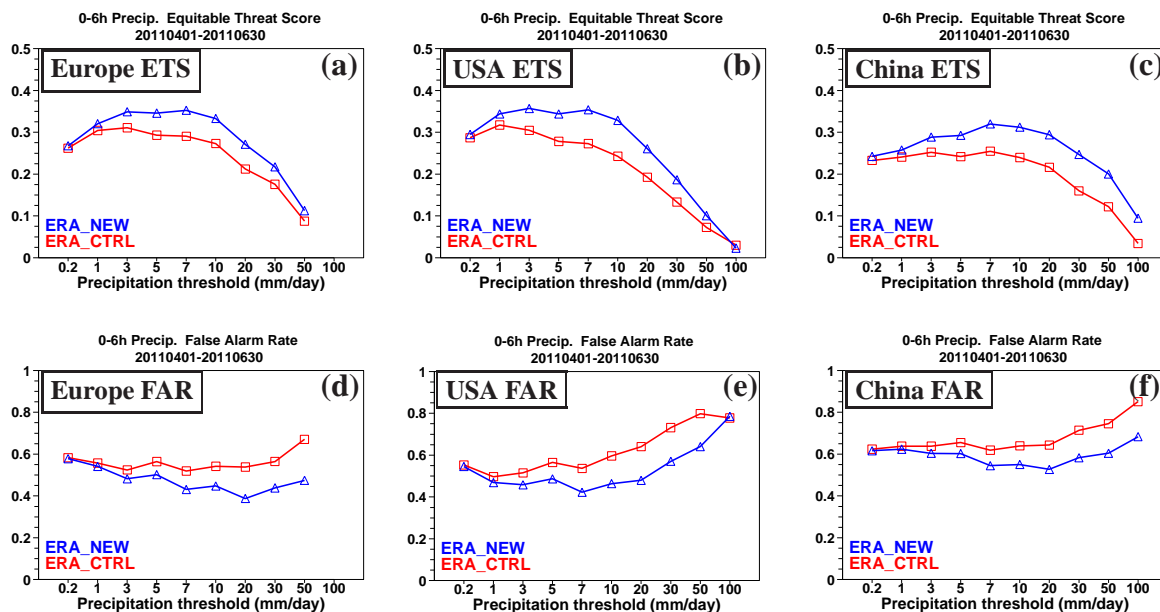


Figure 10: Impact of 4D-Var assimilation of SYNOP RG observations on precipitation forecast scores computed against SYNOP RGs themselves from experiments ERA_CTRL (blue curve and triangles) and ERA_NEW (red curve and squares) in April–June 2011: (a)–(c) Equitable Threat Score and (d)–(f) False Alarm Rate for Europe (left), the USA (middle) and China (right). Scores are displayed for the first 6 hours of the forecasts started at 0000 UTC and as a function of various precipitation intensities (x -axis; in mm day^{-1}). The higher ETS and the lower FAR, the better the forecast.

Figure 10 shows that surface precipitation ETS and FAR during the first six hours of the forecast are substantially improved over the three regions considered and for all precipitation intensities, particularly

above 3 mm day^{-1} (around 25% increase in ETS and 20% drop in FAR). This clearly confirms that the information coming from SYNOP RGs is properly transferred to the model during the 4D-Var assimilation, which supports the idea that genuine precipitation analyses are obtained wherever RGs are available. Beyond the very-short forecast ranges, the positive impact quickly vanishes and becomes neutral (not shown). A similar behaviour was previously identified in the assimilation of ground-based radar data (Lopez 2011) and satellite microwave brightness temperatures (Kelly *et al.* 2008). It is also noteworthy that both ETS and FAR for precipitation intensities below 20 mm day^{-1} are slightly worse over China than over Europe and the USA.

4.2.4 Atmospheric scores against independent observations

The impact of the 4D-Var assimilation of SYNOP RGs on geopotential, temperature and wind vector root-mean-square forecast error (RMSE) computed against radiosonde observations is illustrated in Fig. 11 for the extratropical northern hemisphere, Europe, North America and Asia, since these regions have the highest SYNOP RG data coverage (see Fig. 8). One should emphasize that radiosondes constitute an independent verification dataset in the case of experiments ERA_CTRL and ERA_NEW, in which only SYNOP surface pressure and RGs were assimilated.

Figure 11 clearly shows that the assimilation of SYNOP RGs in 4D-Var brings a systematic and often significant improvement for all plotted parameters, levels and regions. Most forecast ranges up to day 10 benefit from this improvement and the reduction in RMSE is particularly significant over Europe, consistent with its highest density of assimilated RGs (Fig. 8). Only 100 hPa geopotential turns out to be degraded over North America and Asia, yet not significantly (not shown). In contrast, over Europe, 100 hPa geopotential is substantially improved (not shown). Scores in the tropics and over the extratropical southern hemisphere are either positive or neutral (not shown), probably as a result of the smaller number of assimilated rain observations. Close to analysis time, the most significant positive impact is found in the middle and upper troposphere (e.g. 200 hPa wind vector scores in Fig. 11), which suggests that the information contained in the surface precipitation measurements is successfully transferred to upper levels during the 4D-Var minimization.

Additional statistics of 4D-Var analysis departures with respect to independent observations are presented in Fig. 12 using radiosonde geopotential, meridional wind and relative humidity and wind profiler data over Europe, North America and China (Japan for wind profilers). This particular subset of observation types was selected as it exhibited the largest signal. Note that all data used in these statistics were those that passed the 4D-Var first-guess check, even though they were not assimilated. Statistics computed un-screened observations gave similar results. In all panels, the standard deviation of observations–analysis departures is reduced by several percents, reaching up to 8% in the upper troposphere.

Overall, these consistent results provide a clear indication that in the context of a sparse data reanalysis system, assimilating RG data could be very beneficial to the quality of 4D-Var analyses and subsequent forecasts.

4.2.5 Atmospheric forecast scores against operational analyses

Forecast scores against ECMWF operational analyses have also been computed for ERA_CTRL and ERA_NEW and compared to operational forecast scores. One should stress that the operational 4D-Var system is run at high resolution (T1279 L91) and with all conventional and satellite observations available in real-time. As an illustration of these scores, forecast anomaly correlation (FAC) is plotted in Fig. 13

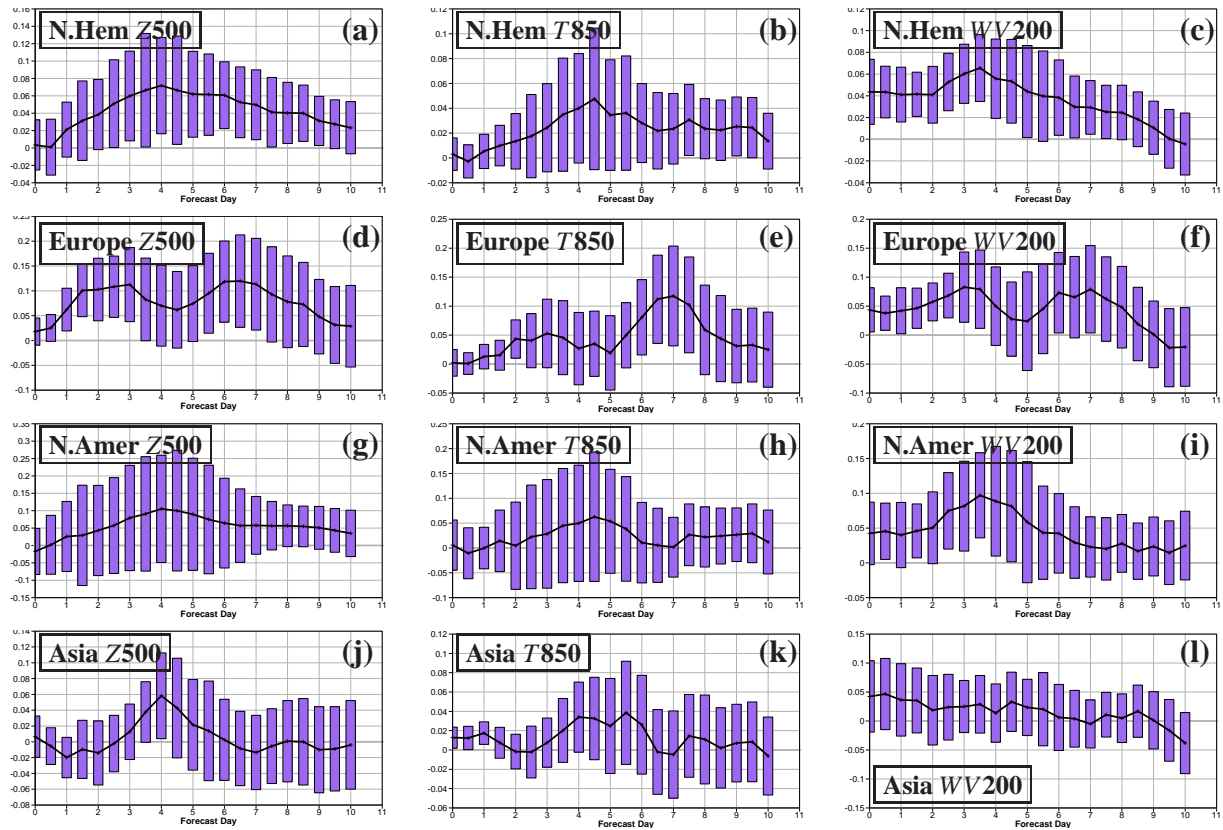


Figure 11: Impact of 4D-Var assimilation of SYNOP RG data on root-mean-square forecast error (RMSE) computed against radiosondes and as a function of forecast range from 0 to 10 days. RMSE changes are plotted for 500 hPa geopotential height (Z500; left panels), 850 hPa temperature (T850; middle panels) and 200 hPa wind vector (WV200; right panels) over four different regions: (a)-(c) extratropical northern hemisphere (N.Hem), (d)-(f) Europe, (g)-(i) North America (N.Amer) and (j)-(l) Asia. Changes shown on y-axis are normalized by the score in experiment ERA_CTRL and positive (resp. negative) values indicate an improvement (resp. degradation) of the score. Purple bars indicate significance at the 95% confidence level. Statistics are valid for the April-June 2011 period.

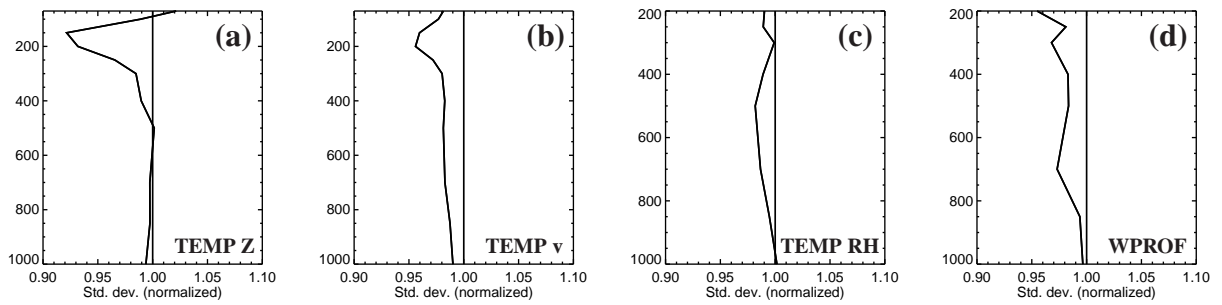


Figure 12: Relative impact of 4D-Var assimilation of SYNOP rain gauge data on the standard deviation of observation–analysis departures computed using (a) geopotential, (b) meridional wind and (c) relative humidity measurements from radiosondes and (d) wind profiler data. The vertical profiles of the ratio of the standard deviations from ERA_NEW and ERA_CTRL is shown. Values below unity along the x-axis indicate an improvement in ERA_NEW. Statistics are aggregated over Europe, North America and China (Japan for wind profilers) and over the period 22 April–30 June 2011.

for geopotential, temperature and wind vector as a function of forecast range from 0 to 10 days. First and foremost, Fig. 13 evidences the strong degradation of FAC in ERA_CTRL compared to operations, as expected from the drastic reduction in the number of observations assimilated in 4D-Var (only SYNOP surface pressure data are used in ERA_CTRL). Secondly, the FAC computed for ERA_NEW is always above that of ERA_CTRL for forecast ranges up to day 5. Beyond day 5, the impact of assimilating RGs is still positive, except for 500 hPa geopotential over North America and Asia (panels (g) and (j)) and for 200 hPa wind over North America (panel (i)). The most striking improvement is obtained for Europe at all forecast ranges, which again is related to the higher density of assimilated rainfall observations. Over the southern hemisphere, more poorly sampled by RGs, the impact is either neutral or slightly positive (not shown). These results confirm the overall positive impact coming from the assimilation of SYNOP RGs.

4.2.6 Verification against satellite infrared imagery

As a complementary independent source of verification, simulated satellite $10.8 \mu\text{m}$ brightness temperatures were computed from short-range forecast fields from ERA_CTRL and ERA_NEW and were compared to corresponding Meteosat-9 images obtained from EUMETSAT. The infrared simulation is based on version 10 of the fast Radiative Transfer for TOVS (RTTOV-10; Matricardi *et al.* 2004, Matricardi 2005). Satellite imagery in the $10.8 \mu\text{m}$ channel mainly provides information about cloud top height in cloudy conditions and surface temperature in clear-sky situations. Table 3 gives the mean Meteosat–model bias and correlation coefficient between Meteosat and model calculated over Europe and over the period April–June 2011 from ERA_CTRL and ERA_NEW. Different forecast ranges from 0 (i.e. roughly the analysis) to 24 hours are considered. The systematic negative bias of around -4 K in the forecasts remains almost unchanged in ERA_NEW versus ERA_CTRL and could be caused either by an underestimation of cloud top height or of cloud condensate amount near cloud top in the forecast model, or by deficiencies in the radiative transfer model in cloudy situations. On the other hand, the correlation coefficient clearly gets higher when SYNOP RGs are assimilated, which indicates that the spatial distribution of clouds is improved. This again confirms the potential benefit of assimilating gauge data in a reanalysis context.

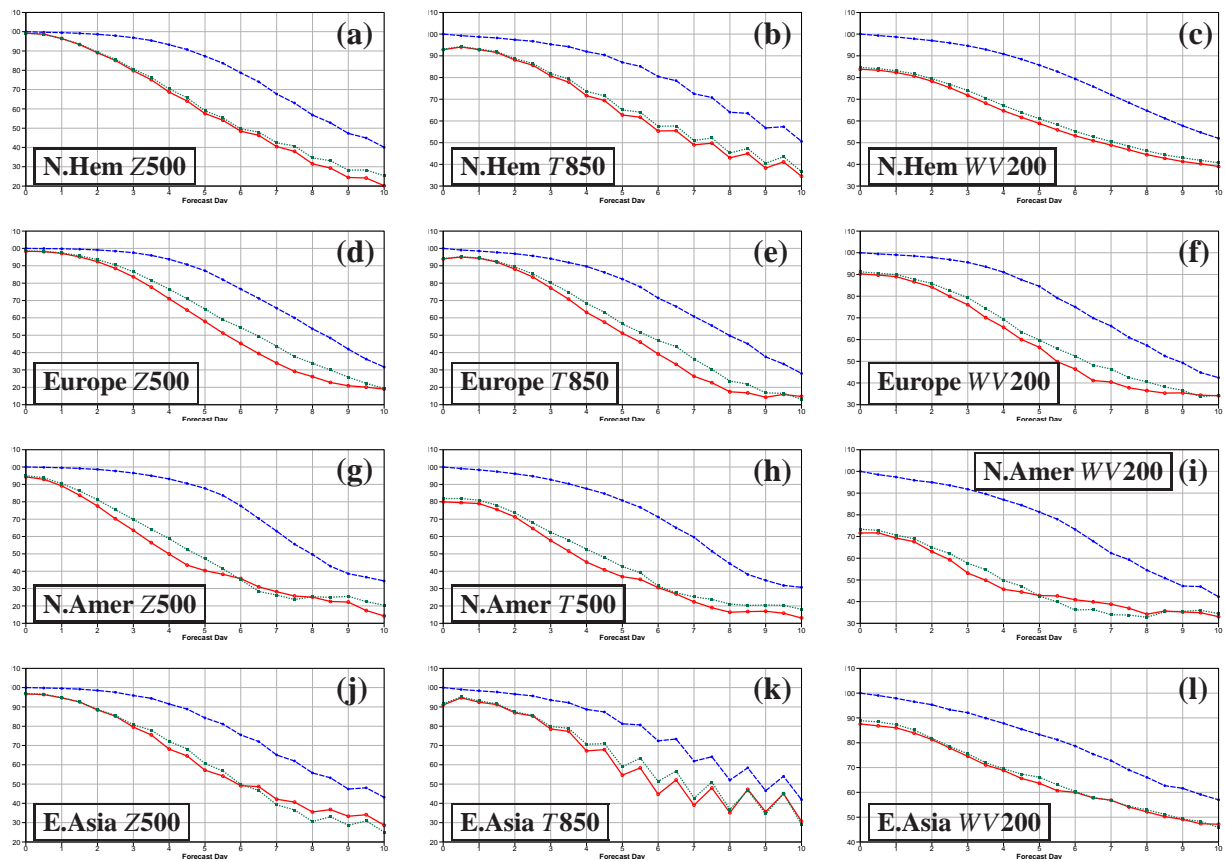


Figure 13: Impact of 4D-Var assimilation of SYNOP rain gauge data on forecast anomaly correlation (FAC) computed against ECMWF operational analyses as a function of forecast range from 0 to 10 days. Blue, red and green curves correspond to ECMWF T1279 operational forecasts, ERA_CTRL and ERA_NEW, respectively. Scores are plotted for 500 hPa geopotential height (Z500; left panels), 850 hPa temperature (T850; middle panels) and 200 hPa wind vector (WV200; right panels) over four different regions: (a)-(c) extratropical northern hemisphere (N.Hem), (d)-(f) Europe, (g)-(i) North America (N.Amer), and (j)-(l) East Asia (E.Asia). Note that over North America 500 hPa T is shown instead of 850 hPa T. The higher FAC, the better the forecast. Statistics are valid for the April-June 2011 period.

	FC+0h		FC+6h		FC+12h		FC+18h		FC+24h	
	Bias	Corr.	Bias	Corr.	Bias	Corr.	Bias	Corr.	Bias	Corr.
ERA_CTRL	-4.12	0.74	-4.46	0.86	-3.53	0.75	-5.46	0.73	-4.84	0.74
ERA_NEW	-4.27	0.80	-4.53	0.93	-3.55	0.79	-5.46	0.78	-4.77	0.75

Table 3: Validation of $10.8 \mu\text{m}$ brightness temperatures simulated from ERA_CTRL and ERA_NEW against Meteosat-9 satellite imagery over Europe. Forecast ranges vary between 0 and 24 hours (every 6 hours) and are given on the top row. Mean Meteosat-model bias (in K) and correlation coefficient (Corr.) between Meteosat and model are valid for the period April-June 2011. The sample size for each forecast range slightly exceeds 500000.

4.3 Results from operations-like experiments

In these experiments, SYNOP RGs were assimilated together with all other observations routinely available in ECMWF's operational system, which includes all conventional and satellite data. Unsurprisingly, the general impact of the gauge data on analyses and forecast performance turned out to be much more modest than in the data-sparse experiments presented in section 4.2. This is because SYNOP RGs have to compete with all other observations and because gauges are mainly available in already well-observed regions. It is noteworthy that similar conclusions were drawn in Lopez and Bauer (2007) and Lopez (2011) for ground-based precipitation radar data over the USA. This usually neutral impact of SYNOP RG data on atmospheric forecast scores against radiosonde observations is illustrated in Fig. 14 for 500 hPa geopotential and 850 hPa temperature over the northern hemisphere extratropics.

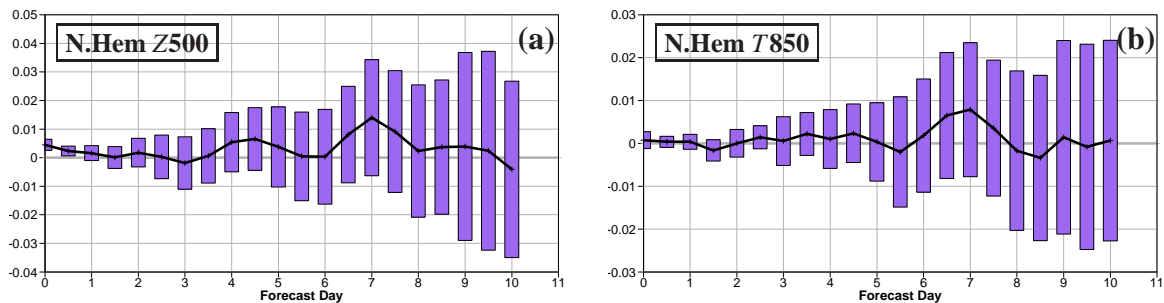


Figure 14: Same as in Fig. 11, but for experiments OPER_NEW versus OPER_CTRL and for the northern hemisphere extratropics only. Statistics are valid for April-May 2011.

However, there is still a hint that short-range forecasts of surface precipitation are slightly improved over Europe, North America and China, as shown in Fig. 15: ETS is increased while FAR is reduced, especially for rain intensities between 20 and 50 mm day⁻¹. Even though the latter verification against SYNOP RGs themselves cannot be considered as independent, Fig. 15 indicates that 4D-Var can successfully extract some information from RG data.

As a conclusion, the benefits of assimilating SYNOP RGs are expected to be smaller in ECMWF's operations than in the context of a future reanalysis of the early or mid-20th century.

5 Remaining issues and future improvements

As already mentioned in section 2.1.3, the formulation of RG representativity error used in the experiments is rather crude since it only depends on the resolution used in the superobbing, on the time of the year and on a rough distinction between mid-latitudes and tropics. Ideally and as shown in Lopez *et al.* (2011), a dependence of representativity error on the grid-box mean observed rain amount itself would be desirable. Unfortunately, the latter quantity is not known in practice. One would also wish to include a dependence of representativity error on the type of observed meteorological situation (e.g. convective versus stratiform). However such additional information, which might be obtained from other observational sources such as geostationary satellite imagery today, would not be available in reanalyses of

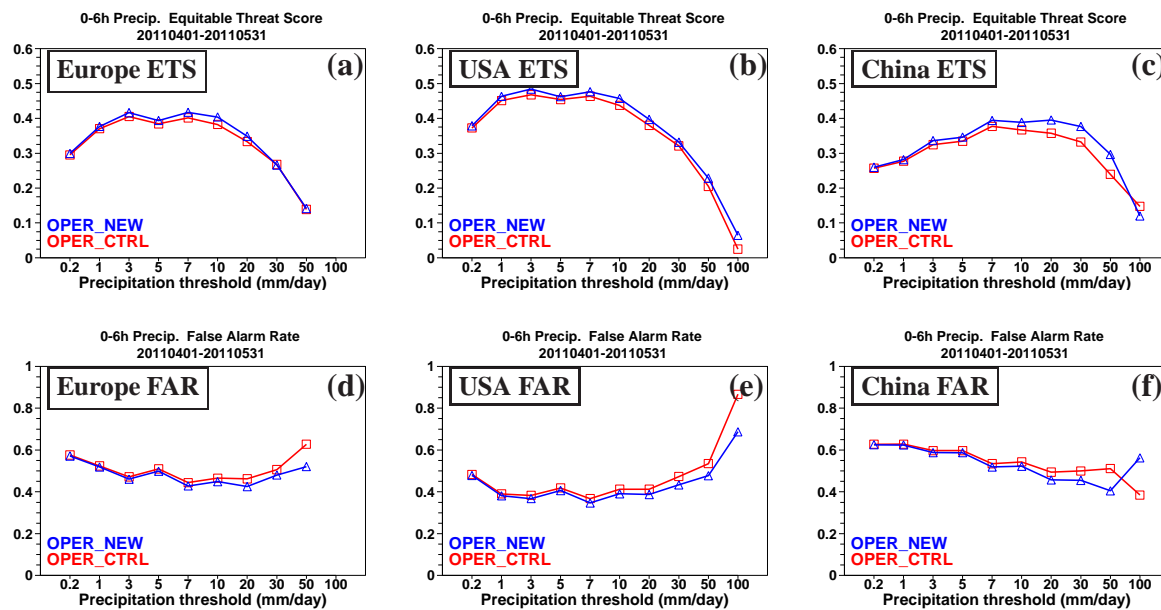


Figure 15: Same as in Fig. 10, but for experiments *OPER_NEW* versus *OPER_CTRL* and for April-May 2011.

data-sparse periods of the past. Furthermore, any given 6-hourly accumulation period might be affected by more than one type of weather condition, for instance in the case of a fast-moving mid-latitude cloud system. This argument would be even more relevant when 12 or 24-hour precipitation accumulations are to be assimilated. It is therefore not clear how to obtain flow-dependent RG representativity errors, hence the usage of a simpler representativity error formulation.

In other respects, because the standard 4D-Var 12-hour window (as used here) starts either at 2100 UTC or 0900 UTC and since SYNOP RG observations consist of 6-hour accumulations between 0000, 0600, 1200 and 1800 UTC, only half of the available gauge data were actually assimilated in the experiments presented here. In the future, shifting the 4D-Var window by three hours could double the usage of SYNOP RG data, with no noticeable extra cost.

In addition, the limited worldwide standardization of rain gauge measurements and the frequent unavailability of metadata may introduce some uncertainty in the wind-induced error bias correction described in section 2.2.1.

The present study strongly suggests that the assimilation of historical RG observations in a future ECMWF reanalysis of the early or mid-20th century could lead to a significant improvement in the quality of those reanalyses and forecasts initiated from these. However, some uncertainties remain regarding older RG observations.

First, the types of RGs used in the past are likely to differ from those used over recent decades. Information about their characteristics and installation protocol (e.g. height above ground, dimensions, shape, surroundings) will probably be even less available than for modern instruments. The variety of RG types might actually be even larger than today's. In particular, this might make the computation of the wind-induced bias correction more uncertain.

Secondly, obtaining older RG accumulations at a frequency shorter than 24 hours is expected to be difficult. In this case, new assimilation experiments will need to be performed to assess whether 4D-Var can still benefit from such longer rain accumulations, particularly with respect to the validity of the linearity assumption, which is so crucial in 4D-Var and less likely to be satisfied in the presence of precipitation (Lopez 2011).

6 Conclusions

In this work, the potential benefits of directly assimilating SYNOP rain gauge 6-hour accumulations in ECMWF's 4D-Var has been assessed in both data-sparse reanalysis-like experiments, mimicking early or mid-20th-century observational coverage, and higher resolution operation-like experiments, with all routinely available observations used. A bias correction for wind-induced error was developed and applied to each RG measurement. Observation error specification involves a simple (and rather crude) parametrization of spatial representativity error (based on the day of the year and on model resolution) and a fixed additional contribution from all other sources of error.

Results from the reanalysis-like experiments clearly indicate that combining SYNOP RGs with surface pressure observations in the data assimilation process brings on significant improvements in the analyses and subsequent forecasts. Even though the positive impact on precipitation itself is relatively short-lived, substantially better forecasts of upper-air geopotential, temperature and wind are obtained up to day 10, at least, especially over the northern hemisphere where SYNOP RG coverage is best. The validation against Meteosat infrared imagery shows that short-range forecast brightness temperatures better correlate with the observations, which suggests that even cloud fields can benefit from the assimilation of rain gauges when other available observations are sparse.

In the operations-like experiments, assimilating SYNOP RG observations together with all other observations leads to an overall neutral impact on atmospheric analyses and forecast scores. Such a limited impact can be expected given the competition between gauges and other observation types, especially radiosondes. However, 4D-Var still seems to be able to successfully extract information from the additional RG data.

These findings advocate the use of historical RG data in future ECMWF's reanalyses covering data-poor periods of the past. However, to achieve this, further testing and developments will be needed to increase rain gauge usage by shifting the 4D-Var assimilation window and to be able to assimilate 12 or 24-hour rather than 6-hour rain accumulations. Quality control might also turn out to be an issue for older RG observations, due to the lack of information about instrument characteristics and set-up. But still, in view of the potential gain, further efforts should be devoted to overcome these problems over the coming months.

Acknowledgements

Special thanks should go to my colleagues Paul Poli and Dick Dee for their help to set-up the reanalysis-type experiments and their comments during this work. I am also very grateful to Alan Geer, Peter Bauer and Anton Beljaars for their internal review of the manuscript. EUMETSAT are acknowledged for providing the Meteosat infrared imagery via EUMETCast.

APPENDIX 1

List of abbreviations used in the text

ECMWF	=	European Centre for Medium-range Weather Forecasts
EUMETSAT	=	European Organisation for the Exploitation of Meteorological Satellites
NCEP	=	National Centers for Environmental Prediction (USA)
MODIS	=	MODerate resolution Imaging Spectroradiometer
SSM/I	=	Special Sensor Microwave Imager
TRMM-PR	=	Tropical Rainfall Measuring Mission - Precipitation Radar

APPENDIX 2

Rain gauge representativity error formulation

In this study, each precipitation superob to be assimilated in 4D-Var is obtained by averaging individual rain gauges inside the corresponding model grid box. Based on Lopez *et al.* (2011) and Morrissey *et al.* (1995), the representativity error, σ_{rep} , assigned to each precipitation superob (in terms of $\ln(RR6h + 1)$) is specified as

$$\sigma_{rep}^2 = \tilde{\sigma}_{rep}^2 VRF[\rho(d)] \quad (10)$$

where $\tilde{\sigma}_{rep}$ is the representativity error of a single rain gauge and VRF is the so-called variance reduction factor. Using Eq.(14) of Morrissey *et al.* (1995), VRF is expressed as a function of $\rho(d)$, the spatial correlation between two rain gauges separated by the distance d . According to Lopez *et al.* (2011), the representativity error for a single rain gauge is computed as

$$\tilde{\sigma}_{rep}(D) = \sigma_0 + \Delta\sigma \sin \left\{ \frac{\pi}{2} \left(\frac{D - 112}{91} \right) + \delta_{hemis} \pi \right\} \quad (11)$$

where D is the day of the year and δ_{hemis} is equal to 0 for the northern hemisphere and 1 for the southern hemisphere. Parameters σ_0 and $\Delta\sigma$ depend on model grid resolution and geographical location according to Table 4. Here, tropics are assumed to extend between 25°S and 25°N and mid-latitudes between 25° and 60° in both hemispheres.

Model grid resolution	Mid-latitudes		Tropics	
	σ_0	$\Delta\sigma$	σ_0	$\Delta\sigma$
15 km	0.220	0.070	0.290	0
40 km	0.285	0.085	0.370	0
80 km	0.350	0.100	0.450	0

Table 4: Values of the two parameters σ_0 and $\Delta\sigma$ used in the parametrization of representativity error for $\ln(RR6h + 1)$ (see Eq. (11)), for various model grid resolutions and for mid-latitudes and tropics.

In Eq. (10), the spatial correlation between rain gauges is parametrized as

$$\rho(d) = \exp [b(M) d^{c(M)}] \quad (12)$$

where d is the separation distance (in km) and $b(M)$ and $c(M)$ are coefficients which depend on the month of the year, M , according to

$$b(M) = b_0 + \Delta b \sin \left\{ \frac{\pi}{2} \left(\frac{M - m_b}{\Delta m_b} \right) + \delta_{hemis} \pi \right\} \quad (13)$$

$$c(M) = c_0 + \Delta c \sin \left\{ \frac{\pi}{2} \left(\frac{M - m_c}{\Delta m_c} \right) + \delta_{hemis} \pi \right\} \quad (14)$$

Coefficients b_0 , Δb , m_b , Δm_b and c_0 , Δc , m_c , Δm_c are given in Table 5, for both mid-latitudes and tropics. In the tropics, b and c are assumed to be constant throughout the year.

Coefficient	Mid-latitudes	Tropics
b_0	-0.056	-0.164
Δb	-0.036	0
m_b	4.803	/
Δm_b	2.481	/
c_0	0.672	0.623
Δc	-0.078	0
m_c	4.711	/
Δm_c	2.548	/

Table 5: Values of the eight coefficients used to describe the monthly variations of the fitting coefficients b and c for spatial correlations of $\ln(RR6h + 1)$ (see Eq. (12), Eq. (13) and Eq. (14)).

More details and graphs of the latter functions can be found in Lopez *et al.* (2011).

APPENDIX 3

Precipitation scores used in this study are the Equitable Threat Score (ETS) and the False Alarm Rate (FAR), defined as follows

$$ETS = \frac{H - H_e}{H + M + F - H_e} \quad (15)$$

$$FAR = \frac{F}{H + F} \quad (16)$$

where H is the number of correct hits, M is the number of misses and F is the number of false alarms. H_e is the number of correct hits purely due to random chance and is computed as

$$H_e = \frac{(H + F)(H + M)}{N} \quad (17)$$

where N is the sample size.

References

- Andersson, E. and Järvinen, H. (1999). Variational quality control. *Q. J. R. Meteorol. Soc.*, 125:697–722.
- Bauer, P., Geer, A. J., Lopez, P., and Salmond, D. (2010). Direct 4D-Var assimilation of all-sky radiances. Part I: Implementation. *Q. J. R. Meteorol. Soc.*, 136:1868–1885.
- Benedetti, A. and Janisková, M. (2008). Assimilation of MODIS Cloud Optical Depths in the ECMWF Model. *Mon. Weather Rev.*, 136:1727–1746.
- Benedetti, A., Lopez, P., Bauer, P., and Moreau, E. (2005). Experimental use of TRMM precipitation radar observations in 1D+4D-Var assimilation. *Q. J. R. Meteorol. Soc.*, 131:2473–2495.
- Caumont, O., Ducrocq, V., Wattrelot, E., Jaubert, G., and Pradier-Vabre, S. (2010). 1D+3D-Var assimilation of radar reflectivity data: a proof of concept. *Tellus*, 62A:173–187.
- Caya, A., Sun, J., and Snyder, C. (2005). A Comparison between the 4DVAR and the Ensemble Kalman Filter Techniques for Radar Data Assimilation. *Mon. Weather Rev.*, 133:3081–3094.
- Ciach, G. J. (2003). Local Random Errors in Tipping-Bucket Rain Gauge Measurements. *J. Atmos. Oceanic Technol.*, 20:752–759.
- Courtier, P., Thépaut, J.-N., and Hollingsworth, A. (1994). A strategy for operational implementation of 4D-Var using an incremental approach. *Q. J. R. Meteorol. Soc.*, 120:1367–1388.
- Dee, D. P. and Uppala, S. (2009). Variational bias correction of satellite radiance data in the ERA-Interim reanalysis. *Q. J. R. Meteorol. Soc.*, 135:1830–1841.
- Ducrocq, V., Ricard, D., Lafore, J.-P., and Orain, F. (2002). Storm-scale numerical rainfall prediction for five precipitating events over France: On the importance of the initial humidity field. *Weather Forecast.*, 17:1236–1256.
- Fisher, M. (2004). Generalized frames on the sphere, with application to the background error covariance modelling. In *Proceedings of the ECMWF Seminar on recent developments in numerical methods for atmospheric and ocean modelling, 6-10 September 2004*, pages 87–102. Available from ECMWF, Reading, UK.
- Folland, C. K. (1988). Numerical models of the raingauge exposure problem, field experiments and an improved collector design. *Q. J. R. Meteorol. Soc.*, 114:1485–1516.
- Geer, A. J. and Bauer, P. (2011). Observation errors in all-sky data assimilation. *Q. J. R. Meteorol. Soc.*, 137:2024–2037.
- Geer, A. J., Bauer, P., and Lopez, P. (2010). Direct 4D-Var assimilation of all-sky radiances. Part II: Assessment. *Q. J. R. Meteorol. Soc.*, 136:1886–1905.
- Ide, K., Courtier, P., Ghil, M., and Lorenc, A. C. (1997). Unified Notation for Data Assimilation: Operational, Sequential and Variational. *J. Meteorol. Soc. Jpn*, 75:181–189.
- Janisková, M., Lopez, P., and Bauer, P. (2011). Experimental 1D+4D-Var assimilation of CloudSat observations. *Q. J. R. Meteorol. Soc.* early view available online, doi:10.1002/qj.988.
- Janisková, M., Mahfouf, J.-F., Morcrette, J.-J., and Chevallier, F. (2002). Linearized radiation and cloud schemes in the ECMWF model: Development and evaluation. *Q. J. R. Meteorol. Soc.*, 128:1505–1527.

- Kelly, G. A., Bauer, P., Geer, A. J., Lopez, P., and Thépaut, J.-N. (2008). Impact of SSM/I observations sensitive to moisture, clouds and precipitation on global NWP forecast skill. *Mon. Weather Rev.*, 136:2713–2726.
- Le Dimet, F.-X. and Talagrand, O. (1986). Variational algorithms for analysis and assimilation of meteorological observations: Theoretical aspects. *Tellus*, 38A:97–110.
- Lin, X., Zhang, S. Q., and Hou, A. Y. (2007). Variational Assimilation of Global Microwave Rainfall Retrievals: Physical and Dynamical Impact on GEOS Analyses. *Mon. Weather Rev.*, 135:2931–2957.
- Lopez, P. (2011). Direct 4D-Var Assimilation of NCEP Stage IV Radar and Gauge Precipitation Data at ECMWF. *Mon. Weather Rev.*, 139:2098–2116.
- Lopez, P. and Bauer, P. (2007). “1D+4D-Var” Assimilation of NCEP Stage IV Radar and Gauge Hourly Precipitation Data at ECMWF. *Mon. Weather Rev.*, 135:2506–2524.
- Lopez, P. and Moreau, E. (2005). A convection scheme for data assimilation: Description and initial tests. *Q. J. R. Meteorol. Soc.*, 131:409–436.
- Lopez, P., Ryu, G.-H., Sohn, B.-J., Davies, L., Jakob, C., and Bauer, P. (2011). Specification of rain gauge representativity error for data assimilation. Technical report. ECMWF Technical Memorandum No. 647, available from ECMWF, Reading, UK.
- Macpherson, B. (2001). Operational experience with assimilation of rainfall data in the Met.Office mesoscale model. *Meteorol. Atmos. Phys.*, 76:3–8.
- Mahfouf, J.-F. (1999). Influence of physical processes on the tangent-linear approximation. *Tellus*, 51A:147–166.
- Mahfouf, J.-F., Brasnett, B., and Gagnon, S. (2007). A Canadian Precipitation Analysis (CaPa) Project: Description and Preliminary Results. *Atmosphere-Ocean*, 45:1–17.
- Marécal, V. and Mahfouf, J.-F. (2003). Experiments on 4D-Var assimilation of rainfall data using an incremental formulation. *Q. J. R. Meteorol. Soc.*, 129:3137–3160.
- Matricardi, M. (2005). The inclusion of aerosols and clouds in RTIASI, the ECMWF fast radiative transfer model for the infrared atmospheric sounding interferometer. Technical report. ECMWF Technical Memorandum No. 474, 53 pages, Available from ECMWF, Reading, UK.
- Matricardi, M., Chevallier, F., Kelly, G., and Thépaut, J.-N. (2004). An improved general fast radiative transfer model for the assimilation of radiance observations. *Q. J. R. Meteorol. Soc.*, 130:153–173.
- Morrissey, M. L., Maliekal, J. A., Greene, J. S., and Wang, J. (1995). The uncertainty of simple spatial averages using rain gauge networks. *Water Resour. Res.*, 31:2011–2017.
- Nešpor, V. and Sevruk, B. (1999). Estimation of wind-induced error of rainfall gauge measurements using a numerical simulation. *J. Atmos. Oceanic Technol.*, 16:450–464.
- Orr, A., Bechtold, P., Scinoccia, J., Ern, M., and Janisková, M. (2010). Improved middle atmosphere climate and analysis in the ECMWF forecasting system through a non-orographic gravity wave parametrization. *J. Climate*, 23:5905–5926.

- Sevruk, B. (1974a). Evaporation losses from containers of Hellmann precipitation gauges. *Hydrol. Sci. Bull.*, XIX:231–236.
- Sevruk, B. (1974b). Correction for the wetting loss of a Hellmann precipitation gauge. *Hydrol. Sci. Bull.*, XIX:549–559.
- Sevruk, B. and Klemm, S. (1989). Catalogue of national standard precipitation gauges. Technical report. WMO, Instruments and observing methods, Report No. 39, available from WMO, Geneva, Switzerland, 50 pp.
- Tompkins, A. M. and Janisková, M. (2004). A cloud scheme for data assimilation: Description and initial tests. *Q. J. R. Meteorol. Soc.*, 130:2495–2518.
- Tong, M. and Xue, M. (2005). Ensemble Kalman Filter Assimilation of Doppler Radar Data with a Compressible Nonhydrostatic Model: OSS Experiments. *Mon. Weather Rev.*, 133:1789–1807.
- Treadon, R. E., Pan, H.-L., Wu, W.-S., Lin, Y., Olson, W. S., and Kuligowski, R. J. (2002). Global and Regional Moisture Analyses at NCEP. In *Proceedings of the ECMWF Workshop on Humidity Analysis, 8-11 July 2002*, pages 33–47. Available from ECMWF, Reading, UK.
- Uppala, S. M., Kållberg, P. W., Simmons, A. J., Andrae, U., Bechtold, V. D. C., Fiorino, M., Gibson, J. K., Haseler, J., Hernandez, A., Kelly, G. A., Li, X., Onogi, K., Saarinen, S., Sokka, N., Allan, R. P., Andersson, E., Arpe, K., Balmaseda, M. A., Beljaars, A., Berg, L. V. D., Bidlot, J., Bormann, N., Caires, S., Chevallier, F., Dethof, A., Dragosavac, M., Fisher, M., Fuentes, M., Hagemann, S., Hólm, E., Hoskins, B. J., Isaksen, L., Janssen, P., Jenne, R., McNally, A. P., Mahfouf, J.-F., Morcrette, J.-J., Rayner, N. A., Saunders, R. W., Simon, P., Sterl, A., Trenberth, K. E., Untch, A., Vasiljevic, D., Viterbo, P., and Woollen, J. (2005). The ERA-40 re-analysis. *Q. J. R. Meteorol. Soc.*, 131:2961–3012.
- Vukicevic, T., Sengupta, M., Jones, A. S., and Haar, T. V. (2006). Cloud-Resolving Satellite Data Assimilation: Information Content of IR Window Observations and Uncertainties in Estimation. *J. Atmos. Sci.*, 63:901–919.
- Yang, D., Goodison, B. E., Metcalfe, J. R., Golubev, V. S., Bates, R., Pangburn, T., and Hanson, C. L. (1998). Accuracy of NWS 8” Standard Nonrecording Precipitation Gauge: Results and Application of WMO Intercomparison. *J. Atmos. Oceanic Technol.*, 15:54–68.